



Strain-controlled cyclic deformation behavior of cast Mg–2.99Nd–0.18Zn–0.38Zr and AZ91D magnesium alloys

Peng Zhang¹, Zhenming Li^{1,*}, and Haiyan Yue¹

¹ National Engineering Research Center of Light Alloys Net Forming and State Key Laboratory of Metal Matrix Composite, Shanghai Jiao Tong University, Shanghai 200030, People's Republic of China

Received: 9 October 2015

Accepted: 22 February 2016

Published online:

29 February 2016

© Springer Science+Business Media New York 2016

ABSTRACT

This paper investigates the fatigue properties and deformation behavior of the T6-treated Mg–2.99Nd–0.18Zn–0.38Zr (NZ30K₀₄) and an AZ91D–T6 magnesium alloys with the same grain size. Compared with the AZ91–T6 alloy, the NZ30K₀₄–T6 alloy shows significant increases in mechanical properties, achieving 17 MPa in YS, 51 MPa in UTS, 2.4 % in elongation, and 15 MPa in FS, respectively. The NZ30K₀₄–T6 alloy also shows higher cyclic stress amplitudes in comparison with the AZ91–T6 alloy. This is attributed to increased matrix strength from the higher precipitate strengthening in the NZ30K₀₄–T6 alloy. The cyclic stress amplitude of the AZ91–T6 alloy increases with increasing the number of cycles. For the NZ30K₀₄–T6 alloy, the cyclic stress amplitude first increases and then decreases during cyclic deformation. Hysteresis loops were symmetrical at all total strain amplitudes due to the lessened extents of texture in these cast magnesium alloys and the absence of twinning–detwinning during cyclic deformation. For both AZ91–T6 and NZ30K₀₄–T6 alloys, the cracked slip bands initiate the fatigue cracks and also assist the crack propagation. The Coffin–Manson law and Basquin equation can be used to evaluate the fatigue parameters and predict the LCF lives of both AZ91–T6 and NZ30K₀₄–T6 alloys. The multi-scale fatigue (MSF) life models and the same model parameters were also used to predict the HCF lives of these alloys.

Introduction

Reducing the weight of large components such as automotive wheels and engine blocks is critical to control fuel consumption and reduce emissions. If magnesium alloy materials can endure the cyclical

loading during wheel and engine block operations, by introducing magnesium wheels and engine blocks to replace cast aluminum wheels and engine blocks will apparently improve fuel efficiency and specific power output [1]. Current commercial magnesium alloys such as AZ91 and AM60, can hardly undergo

Address correspondence to E-mail: lizhenming516@163.com

the wheels and engine blocks running stresses and also do not have sufficient fatigue strength for wheel and engine block applications due to the existence of shrinkage [2–4]. As a recently developed magnesium alloy, Mg–Nd–Zn–Zr (NZK) with higher tensile properties [5–7] and fatigue performance [8–11] as well as corrosion resistance [12–14] is very attractive for powertrain and structural application. For this alloy peak-aged at 200 °C for 10–14 h (T6), fine β'' precipitates with DO_{19} structure ($a = 0.64$ nm, $c = 0.52$ nm) are the dominant strengthening phase [5]. It has been reported that T6-treated Mg–2.85Nd–0.18Zn–0.45Zr (actual chemical compositions in wt% except otherwise stated) alloy engine blocks produced by low pressure sand casting (average grain size $d \approx 100$ μm) exhibited high yield strength (~ 160 MPa at room temperature (RT) of ~ 20 °C and ~ 140 MPa at engine running temperature of 150 °C) and fatigue strength (~ 87 MPa at ~ 20 °C and ~ 70 MPa at 150 °C) [15]. The increasing use of cast magnesium components such as wheels and engine blocks under cyclic loading has drawn considerable interest in their fatigue properties and fracture behavior [16–18]. For the castings, both fatigue properties and deformation behavior are mainly depended on casting defects (such as porosities, oxide films, and inclusions) [19–25] and microstructural characteristics (including grain size, second phase particles, solid solution matrix, and precipitates) [26–31]. For magnesium alloy castings, most of fatigue cracks mainly originated from the flaws near or close to the free surface during fatigue test. The fatigue life of these castings is strongly controlled by the maximum flaw as stress concentration site [23]. In the absence of casting defects or when the casting defect is smaller than a critical size [32], fatigue failure of cast magnesium alloys is controlled by crack initiation first within a grain located at surface or subsurface and then propagation from either twin grain boundaries (T4-treated condition) and persistence slip bands (T6-treated condition) [8].

For the Mg–Nd–Zn–Zr alloys, previous studies concerning the fatigue behavior mainly focused on the high cycle fatigue properties and S–N curve type under stress-controlled condition [8–11], no strain-controlled fatigue performance and cyclic deformation behavior of these alloys have been reported. This paper was aimed to study the fatigue properties and deformation behavior of Mg–2.99Nd–0.18Zn–0.38Zr (NZ30K₀₄) magnesium alloy so as to widen practical

applications of this cast alloy. In order to reduce the effect of defects on the fatigue behavior of the castings, a low pressure sand mold (LSM) casting was used to obtain the alloys without casting defects. A commercial AZ91D alloy produced by LSM casting is included as a baseline in this work. The strain-controlled fatigue deformation behavior and the low cycle fatigue (LCF) parameters (such as cyclic strain-hardening exponent, cyclic strength coefficient, fatigue strength coefficient, fatigue strength exponent, fatigue ductility coefficient, and fatigue ductility exponent) of the AZ91-T6 and NZ30K₀₄-T6 alloys were obtained. In addition, the multi-scale fatigue (MSF) life models [32] and the same coefficients obtained from our previous research [33] for T4- and T6-treated Mg–Nd–Zn–Zr alloys were directly used to estimate fatigue life of both AZ91D-T6 and NZ30K₀₄-T6 alloys without casting defects. The data of the AZ91-T6 and NZ30K₀₄-T6 alloys tested at stress-controlled loading were used to confirm the results of the fatigue life prediction based on the MSF life models.

Experimental procedure

Materials and sample preparation

In this work, LSM casting bars of the AZ91 and NZ30K₀₄ alloys were used as the study objects, as shown in Fig. 1. The alloy with actual chemical compositions of Mg–2.99Nd–0.18Zn–0.38Zr was prepared from high purity Mg and Zn, Mg–90Nd, and Mg–30Zr master alloys in an electrical resistance furnace under protective gas consisting of SF₆ and CO₂, and then cast into a metal mold at pouring temperatures of 740 °C and mold temperatures of 200 °C. Similar casting methods were used to obtain the AZ91D alloy samples with actual chemical compositions of Mg–8.92Al–0.85Zn–0.19Mn. An inductively coupled plasma (ICP) technique was used to confirm the actual chemical compositions of the alloys, as shown in Table 1. After casting, both solid

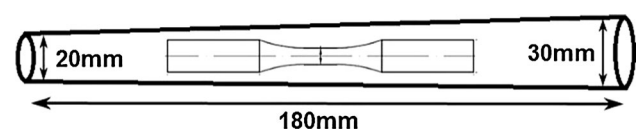


Figure 1 Low pressure sand mold casting bar and sampling location for tensile and fatigue testing.

Table 1 Chemical composition (wt%) of the AZ91D and NZ30K₀₄ alloys

Alloy	Element						
	Al	Zn	Mn	Nd	Zr	Fe	Mg
AZ91D	8.92	0.85	0.19	0	0	0.003	Bal.
NZ30K ₀₄	0	0.18	0	2.99	0.38	0.002	Bal.

solution treatment (540 °C × 10 h) and peak-aging treatment (200 °C × 14 h) (T6) were applied for the NZ30K₀₄ alloy bars. The samples of the AZ91D alloy were heat-treated at 420 °C for 10 h and then aged at 180 °C for 24 h. Standard round tensile samples based on ASTM B557 (gauge diameter of 6 mm and gauge length of 30 mm) and fatigue samples according to ASTM E466 (gauge diameter of 6 mm and gauge length of 12 mm) were sectioned and machined from the bars. In order to reduce the influence of the sample surface quality on the fatigue test results, low-stress machining and electrolytic polishing (EP) were applied for these fatigue samples.

Tensile testing and fatigue testing

RT tensile testing was performed on a Zwick/Roell-20 kN tensile machine with an attached knife-edge extensometer (25 mm). Stress–strain curves, the ultimate tensile strength (UTS, σ_b), yield strength (YS, $\sigma_{0.2}$), and elongation of the specimens were determined from the tensile test data. All the tests were performed at a tensile rate of 0.5 mm/min and at least four tests were finished for each alloy. The fatigue specimens of the AZ91-T6 and NZ30K₀₄-T6 alloys were tested in a servohydraulic Instron (8805) fatigue machine under strain control at a frequency of 2 Hz and a constant strain rate of $1 \times 10^{-2} \text{ S}^{-1}$. Triangular waveform loading (push–pull, $R = -1$) was performed at total strain amplitudes of 0.2, 0.3, 0.4, 0.5, and 0.6 %, respectively. The strain-controlled tests at lower strain amplitudes (such as 0.2 and 0.3 %) were conducted until 10,000 cycles, and then the tests were changed to stress control (push–pull, $R = -1$, triangular waveform and frequency of 30 Hz). Most fatigue tests were carried out at a zero mean strain (strain ratio $R_s = -1$, completely reversed strain cycle), RT of 20–25 °C, and relative

humidity level of 30–40 %. Stress-controlled high cycle fatigue testing was performed on a SincoTec MAG fatigue machine with a push–pull sinusoidal waveform (stress ratio $R = -1$, frequency of 60 Hz) in ambient air. The fatigue endurance limit at a given number (1×10^7) of cycles to failure was estimated using a method named as load-controlled staircase testing. The calculation method for fatigue strength from staircase testing results was given in Ref. [8] and 5 MPa was chosen as step size. 35–40 specimens were used for push–pull high cycle fatigue test.

Microstructural and fractographic examination

Metallographic samples (sectioned from the fatigue samples) for optical microscopy (OM) were cold mounted, mechanically polished, etched in an acetic-picric solution (20 ml acetic acid, 60 ml ethanol, 1 ml nitric acid, and 19 ml water) and then observed using an Olympus optical microscope. A linear intercept method was applied to calculate the average grain size of the alloys. Fracture surfaces of the fatigue specimens, fatigue crack initiator site, crack propagation region, and overload region were investigated using a ZEISS EVO scanning electron microscope (SEM). The sizes of the grains as the initial crack originating sites were determined in an image analysis software package (Ipwin 32) based on their projected areas, lengths, and the depth from the sample surface [25]. For the multiple crack initiators, the size of the grain as crack initiation site in the crack initiation region was defined as the square root of total area (\sqrt{A}) of the individual maximum crack initiators.

In this work, both direct observation of the specimen surface and replica method using OM at $\times 500$ magnification were used to investigate the fatigue crack initiation and propagation behavior of the alloys. In order to obtain the ratio of crack initiation life/total life (N_i/N_f), the selected fatigue tests were conducted on some samples of both AZ91-T6 and NZ30K₀₄-T6 alloys whose microstructure was revealed by etching. These experiments tested at some given stress amplitudes were interrupted at selected number of cycles to collect replicas of the specimen surface. The N_i/N_f ratio at different stress amplitudes were obtained by means of these observations.

Results and discussion

Microstructure and tensile properties

The typical microstructures of the AZ91-T6 and NZ30K₀₄-T6 alloys produced by LSM casting are shown in Fig. 2. Large discontinuous precipitates along the grain boundaries were observed on AZ91-T6 alloy as shown in Fig. 2a. Figure 3 shows the typical SEM morphologies of the β -Mg₁₇Al₁₂ phase in the AZ91-T6 alloy. The microstructure of the as-cast NZ30K₀₄ alloy mainly consists of a soft α -Mg matrix and some Mg₁₂Nd eutectic compounds along with the grain boundaries. After solid solution treatment, the eutectic compounds have almost dissolved into the matrix. The NZ30K-T6 alloy shows similar microstructure to that of solution-treated one, as shown in Fig. 2b. Some Zr-containing particles can also be seen in the NZ30K₀₄-T6 alloy (indicated by the red arrows in Fig. 2b). It has been reported that these particles formed during solution treatment and their influence on the mechanical properties of the NZ30K-

T6 alloy can be ignored [34]. The micrographs of the β -Mg₁₇Al₁₂ precipitates in the AZ91-T6 alloy and the β'' precipitates in the NZ30K₀₄-T6 alloy are shown in Fig. 4. The discontinuous precipitation of β -Mg₁₇Al₁₂ phase occurs at the aged temperature of 200 °C, which was lamellar structure parallel or perpendicular to the based plane of matrix, nucleated at grain boundaries, and grew into grains (as shown in Fig. 4a) [35]. For the NZ30 K alloy, at the peak-aged condition (200 °C × 14 h), the fine plate-shaped β'' precipitates are the dominant strengthening phase, which may have two kinds of habit planes, $\{1-100\}_\alpha$ and $\{11-20\}_\alpha$ prism planes (as shown in Fig. 4b) [5]. The β'' precipitates in the NZ30K₀₄-T6 alloy are denser and smaller than the β -Mg₁₇Al₁₂ precipitates in the AZ91-T6 alloy. Based on the linear intercept, it is obtained that the average grain size of both AZ91-T6 and NZ30K₀₄-T6 alloys is about 135 μ m, as shown in Table 2. Figure 5 shows the grain size distributions in the AZ91-T6 and NZ30K₀₄-T6 alloys. The distributions of grain size in both AZ91 and NZ30K₀₄ alloy samples are similar, which is close to Gaussian

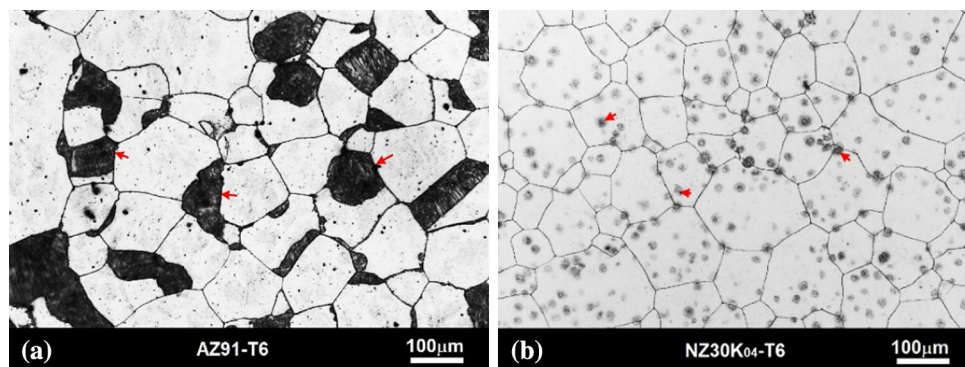
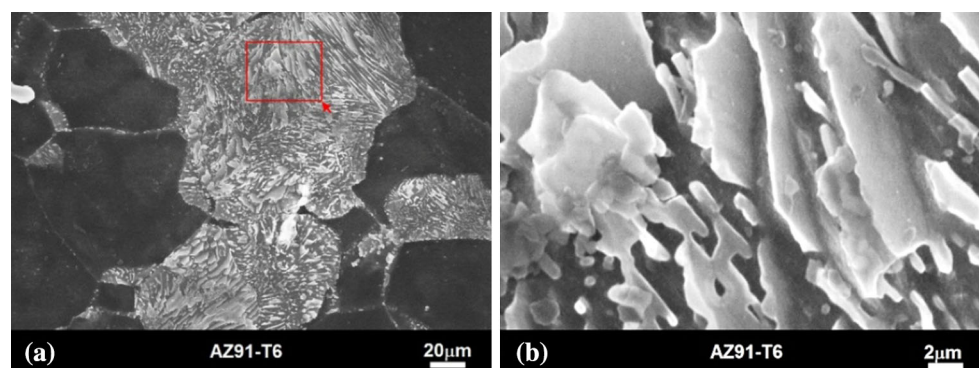


Figure 2 Optical micrograph image of the **a** AZ91D-T6 alloy and **b** NZ30K₀₄-T6 alloy. Large discontinuous precipitates and Zr-containing particles are also observed at grain boundaries of the

AZ91-T6 alloy and grain interiors of the NZ30K₀₄-T6 alloy (indicated by the *arrows*), respectively.

Figure 3 **a** SEM morphologies of β -Mg₁₇Al₁₂ phase in the AZ91-T6 alloy. The location of image **b** is shown by the square in image **(a)**.



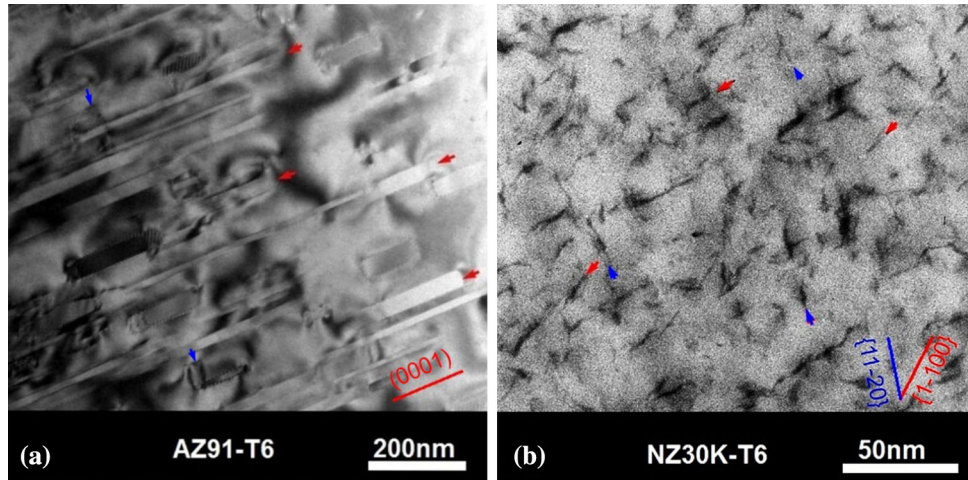


Figure 4 **a** TEM bright-field image showing precipitates observed from $[11\bar{2}0]_{\alpha}$ zone axis of the AZ91-T6 alloy and **b** from $[0001]_{\alpha}$ zone axis of the NZ30K-T6 alloy [5]. The β - $Mg_{17}Al_{12}$ phase in the AZ91-T6 alloy was lamellar structure

parallel or perpendicular to the basal plane of matrix, and the β'' phase in the NZ30K₀₄-T6 alloy have two kinds of habit planes $\{1\bar{1}00\}_{\alpha}$ and $\{11\bar{2}0\}_{\alpha}$ prism planes.

Table 2 Grain size, tensile properties, and stress-controlled high cycle fatigue properties of the AZ91D-T6 and NZ30K₀₄-T6 alloys

Alloy	Grain size (μm)	YS (MPa)	UTS (MPa)	A (%)	FS (MPa)	FS/YS ($\sigma_f/\sigma_{0.2}$)	FS/UTS ($\sigma_f/\sigma_{0.2}$)	<i>n</i>	<i>K</i> (MPa)
AZ91D	135	131	234	4.8	74	0.56	0.32	0.2	450
NZ30K ₀₄	136	148	285	7.2	89	0.60	0.31	0.19	487

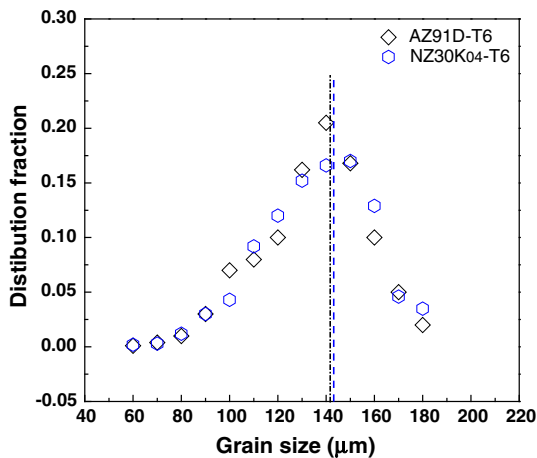


Figure 5 Grain size distribution fraction of the AZ91D-T6 and NZ30K₀₄-T6 alloys.

distribution. These results indicate that for the AZ91-T6 and NZ30K₀₄-T6 alloys, there was no significant difference in average grain size and the distributions of grain size.

The tensile properties obtained for the AZ91-T6 and NZ30K₀₄-T6 alloys are listed in Table 2. The NZ30K₀₄-T6 alloy samples exhibit higher tensile properties (YS of ~ 148 MPa, UTS of ~ 284 MPa, elongation of ~ 7.2 %), improved by ~ 17 MPa in YS, ~ 51 MPa in UTS, and ~ 2.4 % in elongation, respectively, in comparison with those of the AZ91-T6 alloy samples with the same grain size (YS of ~ 131 MPa, UTS of ~ 234 MPa, and elongation of ~ 4.8 %). Generally, the stress–strain curves of magnesium alloys in plastic deformation stage can be expressed using the Hollomon equation ($\sigma = K\varepsilon^n$). The true stress—logarithmic plastic strain curves of both AZ91-T6 and NZ30K₀₄-T6 alloys are shown in Fig. 6a. To obtain the strain-hardening exponent (*n*) and the strain-hardening coefficient (*K*) of the two alloys, the log (true stress)—log (logarithmic plastic strain) data over a strain range from about 0.01 up to instability is plotted in Fig. 6b. The constant values (for AZ91-T6: *n* of ~ 0.2 and *K* of ~ 450 MPa, for NZ30K₀₄-T6: *n* of ~ 0.19 and *K* of ~ 487 MPa) for these alloys were obtained by fitting the linear relationship (as shown in Table 2).

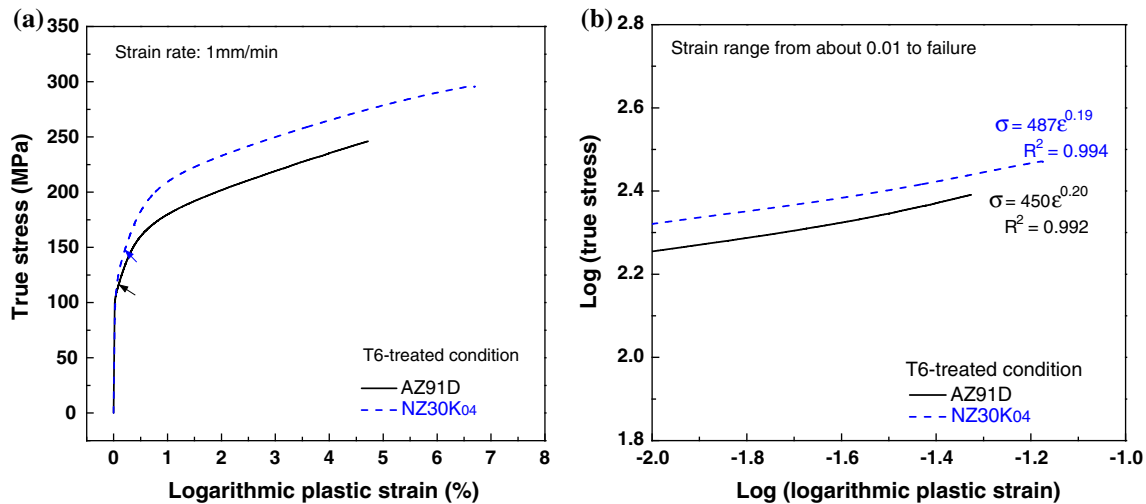


Figure 6 a True stress–logarithmic plastic strain curves showing the flow behavior of the AZ91D-T6 and NZ30K₀₄-T6 alloys. b Determination of n values for the AZ91D-T6 and NZ30K₀₄-T6

alloys by linear fit to the log true stress–log logarithmic plastic strain curves.

Strain-controlled fatigue behaviors

Hysteresis loops

Figure 7 shows the hysteresis loops of the AZ91-T6 and NZ30K₀₄-T6 alloys for selected cycles (first and half-life) at total strain amplitudes of 0.2 and 0.6 %. It is clearly seen that for both AZ91-T6 and NZ30K₀₄-T6 alloys tested at different total strain amplitudes, the cyclic compressive stress is almost the same as the cyclic tensile stress. During cyclic deformation, the shape of the hysteresis loops of the alloys tested at different total strain amplitudes is nearly symmetrical. This behavior indicates that for these casting magnesium alloys such as AZ91 and NZ30K₀₄, the shape of hysteresis loops is not significantly affected by the total strain amplitudes. In contrast, the deformation asymmetry in some wrought magnesium alloys [16] at different total strain amplitudes was observed from the hysteresis loops. It was suggested that this behavior is mainly attributed to the activity of twinning in compression during unloading and subsequent detwinning in tension during loading [36–39]. In this work, the total strain amplitude and the number of cycles do not significantly influence the shape of hysteresis loops, due to the lessened extents of texture in these casting magnesium alloys [40] and the absence of twinning–detwinning in the entire fatigue process [17].

Cyclic stress responses

Variation of cyclic stress amplitude with the number of cycles for AZ91-T6 and NZ30K₀₄-T6 alloys (at the total strain amplitudes of 0.2, 0.4 and 0.6 %) are shown in Fig. 8a. It is clearly seen that the cyclic stress amplitude of both AZ91-T6 and NZ30K₀₄-T6 alloys increases with the total strain amplitude increasing. For the AZ91-T6 alloy, the stress amplitude (in these strain-controlled tests) increases with the increase of the number of cycles, and more so when at higher strain amplitude tests (>0.3 %). In contrast, the stress amplitude of the T6-treated NZ30K₀₄ alloy remains almost constant at the lower total strain amplitudes (such as 0.2 %). At the higher total strain amplitude (>0.4 %), however, the hardening curves of this alloy (in these strain-controlled tests) all show clearly cyclic softening after the cyclic stress reaches a maximum value. Since cracks were detected on the specimen surface after the stress amplitude reached a maximum, it is confirmed that softening is also caused by surface crack initiation. Compared with the AZ91D-T6 alloy, the T6-treated NZ30K₀₄ alloy shows significant improvements in cyclic stress amplitudes, especially a significant increase of them at higher total strains (as shown in Fig. 8a). For example, at the total strain amplitude of 0.6 %, the maximum cyclic stress amplitude of the NZ30K₀₄-T6 alloy (~194 MPa) represents about

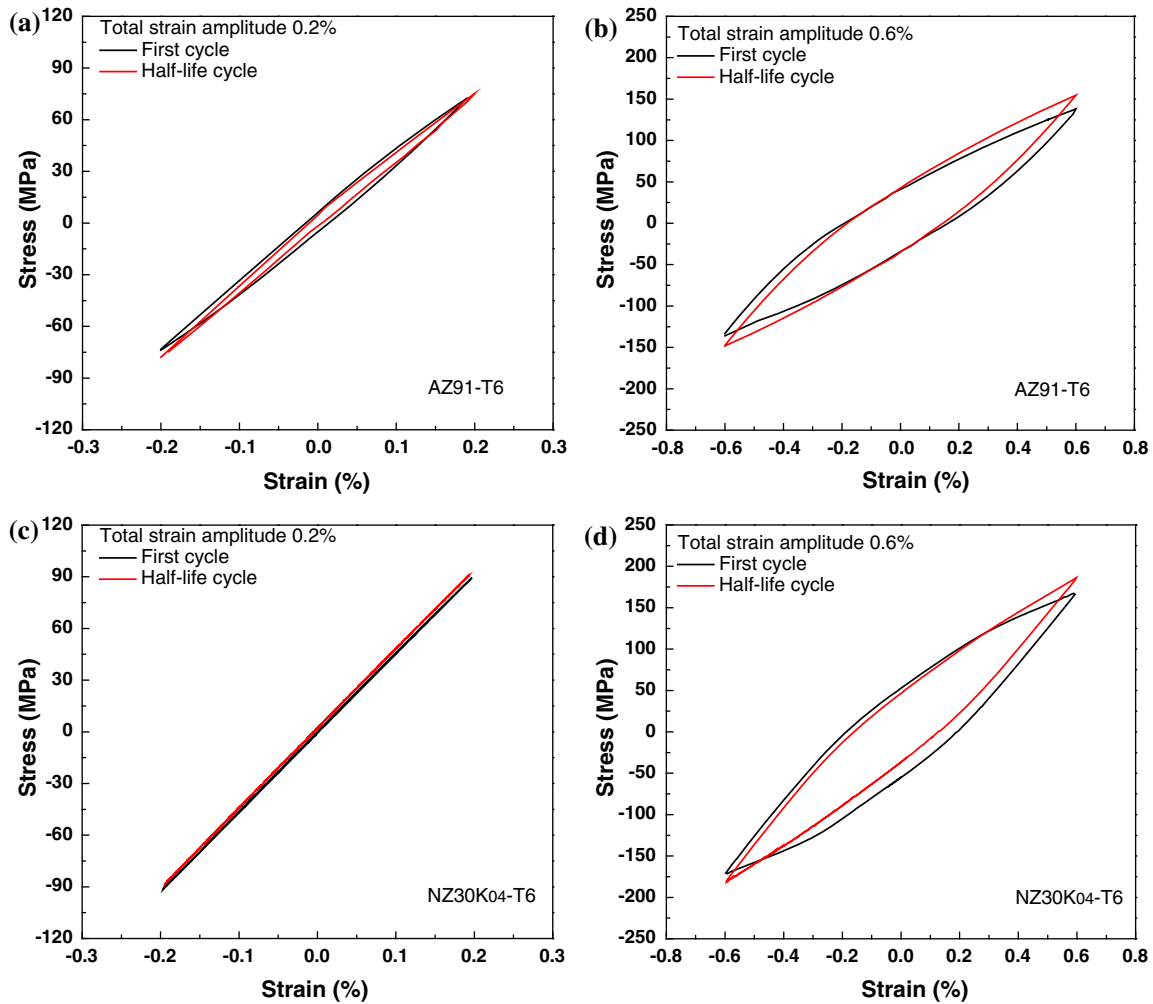


Figure 7 Typical hysteresis loops for both AZ91-T6 (a, b) and c, d NZ30K₀₄-T6 alloys at the first cycle and half-life cycle at different total strain amplitudes of 0.2% (a, c) and 0.6% (b, d).

34 MPa increases compared with that of the AZ91D-T6 alloy (~160 MPa).

In order to discern the cyclic strain-hardening or softening mechanism, the monotonic true stress versus true strain and the cyclic stress–strain curves of both AZ91-T6 and the NZ30K₀₄-T6 alloys are shown in Fig. 8b. Tensile flow stress and cyclic stress amplitudes of the two alloys at total strain value of 0.2 and 0.6 % are summarized in Table 3. The results clearly indicate that the flow stress of the NZ30K₀₄-T6 alloy are apparently higher compared with that of the AZ91-T6 alloy when they have the same grain size. The initial cyclic stress amplitudes of the AZ91-T6 and NZ30K₀₄-T6 alloys are about 73 MPa (0.2 %) or 138 MPa (0.6 %), and 90 MPa (0.2 %) or 165 MPa (0.6 %), respectively, which is same to the tensile stress at the total strain values of 0.2 or 0.6 %. With

the cyclic number increasing, both AZ91-T6 and NZ30K₀₄-T6 alloy tested at high total strain amplitudes (>0.2 %) were hardened much more in the cyclic loading condition than in the monotonic loading condition. After 200 cycles, the cyclic stress amplitude of the AZ91-T6 and NZ30K₀₄-T6 alloys increase up to ~154 MPa and ~193 MPa (total strain amplitude of 0.6 %), respectively, which are higher than the flow stresses of these alloys tested at monotonic condition (as shown in Fig. 8b).

Compared with the AZ91-T6 alloy, the NZ30K₀₄-T6 alloy exhibits the higher cyclic hardening behavior. Since the grain size of the AZ91-T6 alloy and the NZ30K₀₄-T6 alloy is similar (average grain size $d \sim 135 \mu\text{m}$), the improvements in cyclic stress amplitude can only be attributed to different characteristic microstructure and hardening mechanism

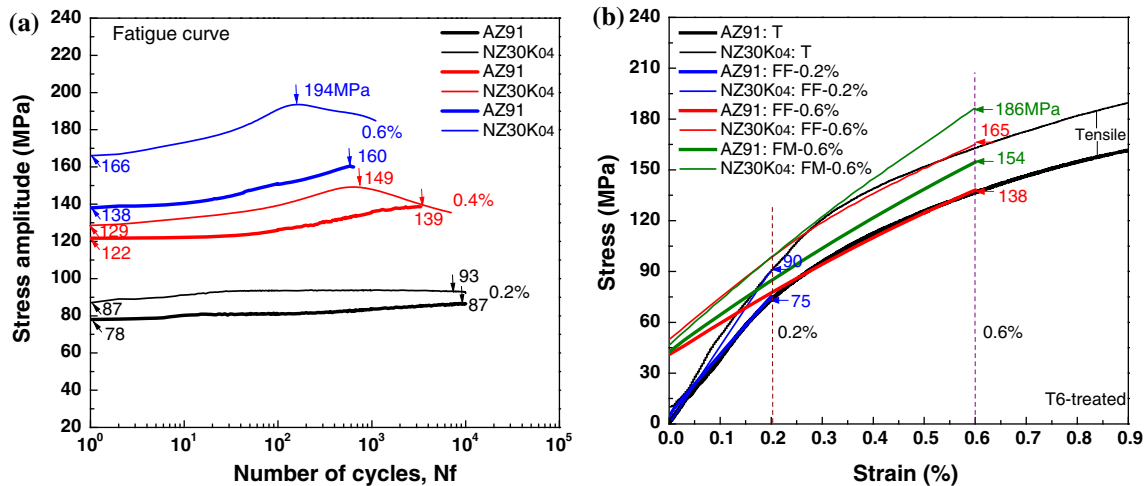


Figure 8 **a** Variation of stress amplitude with the number of cycles for T6-treated AZ91 and NZ30K₀₄ alloys; **b** tensile and fatigue stress–strain curves for both AZ91-T6 and the NZ30K₀₄-

T6 alloys. *T* tensile curve, *FF* hysteresis loops at the first cycle, *FM* hysteresis loops corresponding to the maximum stress amplitude.

Table 3 Tensile strengths and cyclic stress amplitudes of the AZ91-T6 and NZ30K₀₄-T6 alloys at total strain values of 0.2 and 0.6 %

Total strain values (%)	Alloy	Tensile flow stress (MPa)	Cyclic stress amplitude (MPa)		
			Initiation value	Half-life value	Maximum value
0.2	AZ91	73	75	86	87
	NZ30K ₀₄	90	90	93	93
0.6	AZ91	137	138	156	160
	NZ30K ₀₄	163	165	186	194

during cyclic deformation in two alloys. The NZ30K₀₄-T6 alloy has higher cyclic strengthening mainly due to the improvement of the matrix strength and higher crack initiation and growth resistances. After the aging treatment, besides the pure Mg (σ_{Mg}) and grain boundary strengthening (σ_{gb}), only precipitates strengthening dominate the hardening behavior of cast AZ91-T6 and NZ30K₀₄-T6 alloys [41]. Compared with the AZ91-T6 alloy, the precipitates in the NZ30K₀₄-T6 alloy are denser and smaller (as shown in Fig. 4). The β'' precipitates hardening in the NZ30K₀₄-T6 alloy is generally much stronger than the β -Mg₁₇Al₁₂ precipitates strengthening in the AZ91-T6 alloy [5]. The increased matrix strength from the precipitate strengthening contributions can increase the matrix resistance to dislocation movement and formation of slip bands as well as decrease the number and size of local plastic of deformation zones in the samples. The interaction of dislocations with grain boundaries decreasing leads to the decrease of the possibility of forming

microcracks in front of the fatigue cracks. Thus, it is believed that increasing matrix strength can decrease not only crack initiation but also crack growth rate.

Change of elastic modulus and cyclic strain resistance

Figure 9 illustrates that the influence of the total strain amplitude on the average elasticity modulus value and the plastic strain amplitude ($\Delta\varepsilon_p/2$) of the AZ91 and NZ30K₀₄ alloys under T6-treated condition, as the function of the number of cycles. It can be clearly seen that the average modulus of the elasticity of both AZ91-T6 and NZ30K₀₄-T6 alloys decreases with increasing total strain amplitude, which is due to the increase of the plastic part of the total strain amplitude. The average modulus of the elasticity of the AZ91-T6 alloy, as shown in Fig. 9a, increases with the number of the cycles increasing. For the NZ30K₀₄-T6 alloy tested at low applied strain amplitudes (such as 0.2, 0.3 and 0.4 %), the average modulus of the elasticity remains almost constant at the entire fatigue

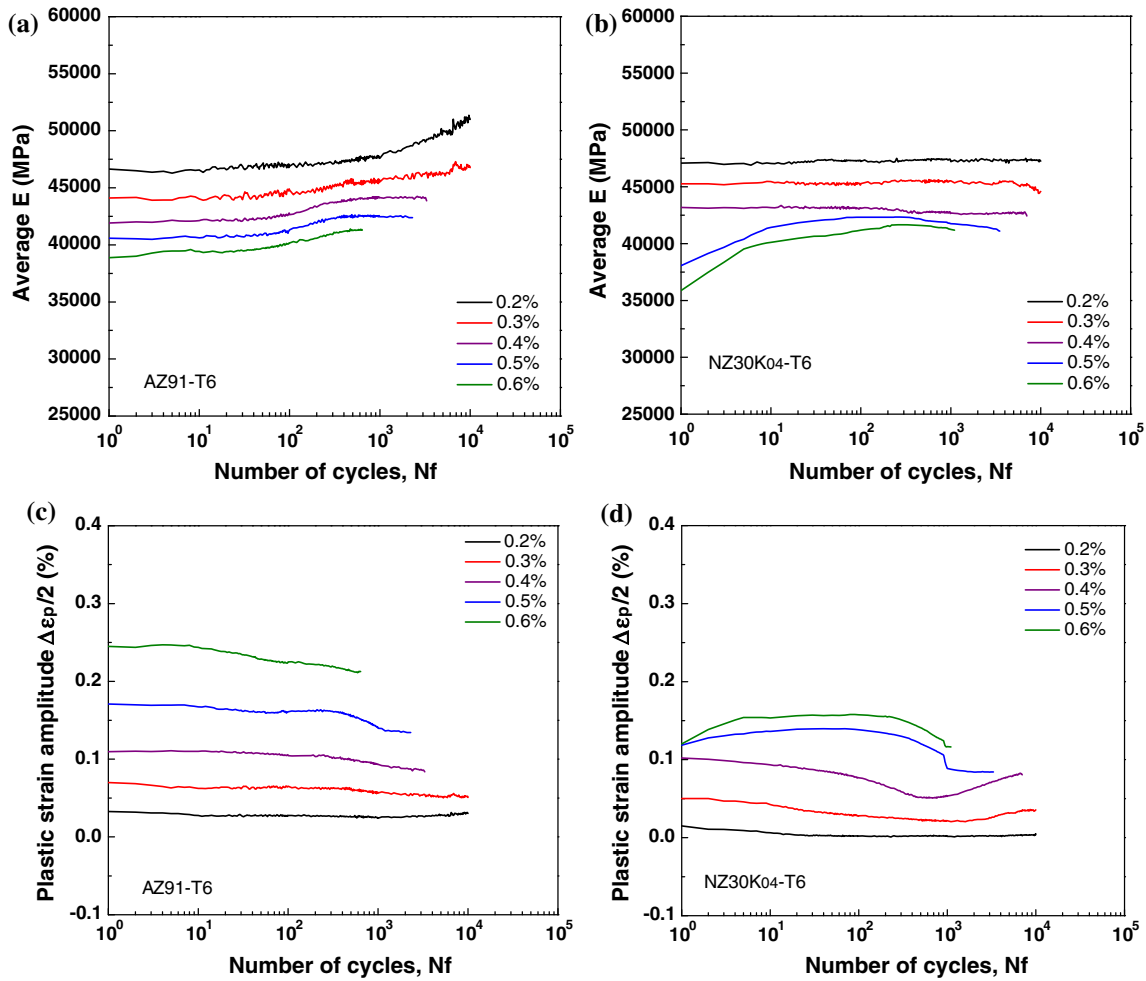


Figure 9 Effect of total strain amplitudes on the average modulus for the **a** AZ91-T6 and **b** NZ30K₀₄-T6 alloys, as a function of the number of cycles. Evolution of plastic strain amplitude in the strain-controlled fatigue tests for the **c** AZ91-T6 and **d** NZ30K₀₄-T6 alloys.

life (as shown in Fig. 9b). At the high strain amplitude (>0.4 %), *E* (average elasticity modulus) of the NZ30K₀₄-T6 alloy first increases and then decreases until failure during fatigue testing.

The variation of the plastic strain amplitude ($\Delta\epsilon_p/2$) of both the AZ91-T6 and NZ30K₀₄-T6 alloys, in Fig. 9c, d, clearly shows that increasing the total strain amplitude increases the value of the plastic strain amplitude. At the low total strain amplitude (such as 0.2 %), the plastic strain amplitude of both AZ91-T6 and NZ30K₀₄-T6 alloys remains nearly constant with the number of the cycle increasing. For the AZ91-T6 alloy, with the total strain amplitude increasing (>0.3 %), the plastic strain amplitude slightly decreases up to failure (Fig. 9c), corresponding to the increase of the cyclic stress amplitude. In contrast, the plastic strain amplitude of the NZ30K₀₄-T6 alloy tested at high total strain

amplitudes (>0.3 %) changes its direction from decrease to increase prior to failure, corresponding to the onset of fatigue crack initiation (Fig. 9d).

Fatigue life and low cyclic fatigue parameters

The strain-life curves of both AZ91-T6 and NZ30K₀₄-T6 alloys are shown in Fig. 10a. It is clearly seen that for these alloys, decreasing the applied total strain amplitude significantly increases the number of the cycles. Fatigue lives of metal materials are correlated with elastic, plastic and total strain amplitudes. The elastic strain amplitude is determined by subtracting plastic strain amplitude from total strain amplitude. Figure 10b shows the total strain fatigue life diagrams for both AZ91-T6 and NZ30K₀₄-T6 alloys. As shown in Fig. 10b, the fatigue life of the AZ91-T6 and NZ30K₀₄-T6 alloys can be described either by the

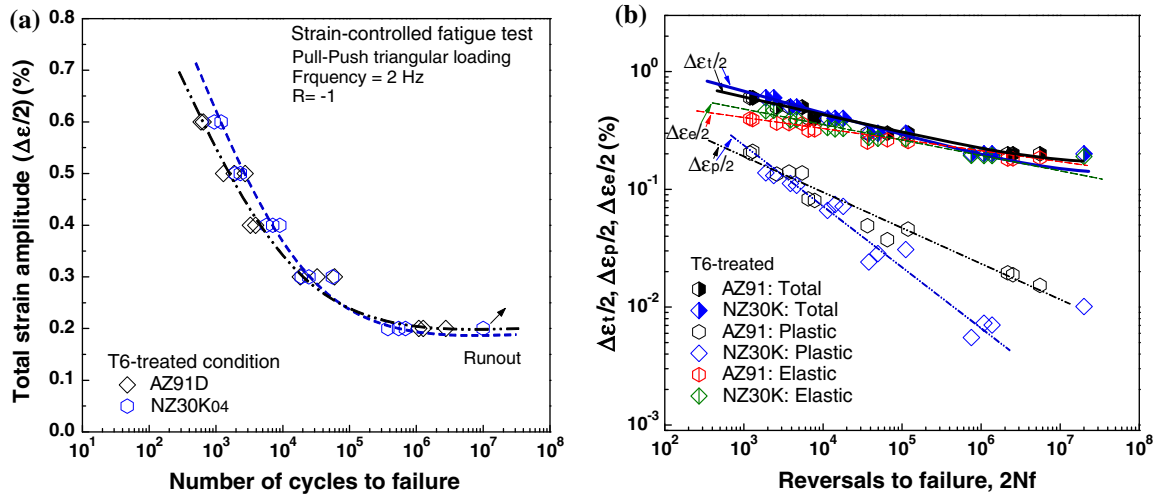


Figure 10 a Total strain amplitude versus life curves of the AZ91-T6 and NZ30K₀₄-T6 alloys. b Total strain fatigue life diagrams for both AZ91-T6 and NZ30K₀₄-T6 alloys. Coffin–Manson and Basquin plots for two alloys were shown in figure.

Coffin–Manson relation (as Eq. 1) [42–45] or the Basquin relation (as Eq. 2) [44–47]:

$$\frac{\Delta\epsilon_p}{2} = \epsilon'_f (2N_f)^c, \tag{1}$$

$$\frac{\Delta\epsilon_e}{2} = \frac{\sigma'_f (2N_f)^b}{E} \tag{2}$$

Therefore, the total strain amplitude of both AZ91-T6 and NZ30K₀₄-T6 alloys can be determined by using Coffin–Manson relation and Basquin laws as [42–48]:

$$\begin{aligned} \frac{\Delta\epsilon_t}{2} &= \frac{\Delta\epsilon_e}{2} + \frac{\Delta\epsilon_p}{2} = \frac{\Delta\sigma}{2E} + \left(\frac{\Delta\sigma}{2K'}\right)^{1/n'} \\ &= \frac{\sigma'_f (2N_f)^b}{E} + \epsilon'_f (2N_f)^c, \end{aligned} \tag{3}$$

where $\Delta\sigma$ is the cyclic stress range, N_f is the fatigue life, and E is the Young’s modulus (modulus of elasticity); $\Delta\epsilon_t$, $\Delta\epsilon_p$ and $\Delta\epsilon_e$ are the total strain range, plastic strain range and elastic strain range, respectively. Material-related constant n' and K' are the cyclic strain-hardening exponent and cyclic strength coefficient, respectively; σ'_f and b are the fatigue strength coefficient and fatigue exponent, respectively; ϵ'_f is the fatigue ductility coefficient and c is the fatigue ductility exponent.

As shown in Fig. 11, by fitting the relationship between $\log(\Delta\sigma/2)$ and $\log(2N_f)$, $\log(\Delta\sigma/2)$ and $\log(\Delta\epsilon_p/2)$, $\log(\Delta\epsilon_p/2)$ and $\log(2N_f)$, $\log(\Delta\epsilon_e/2)$ and $\log(2N_f)$, the related fatigue parameters of both AZ91-T6 and NZ30K₀₄-T6 alloys required for the calculation of fatigue life were calculated and summarized in

Table 4. The results also indicate that both AZ91-T6 and NZ30K₀₄-T6 alloys exhibit significantly higher cyclic strain-hardening exponent value (for AZ91-T6: $n' \approx 0.26$ and for NZ30K₀₄-T6: $n' \approx 0.22$) in comparison with the monotonic strain-hardening exponent values (for AZ91-T6: $n \approx 0.2$ and for NZ30K₀₄-T6: $n \approx 0.19$).

Stress-controlled fatigue performance

In this work, the stress-controlled high cycle fatigue properties of both AZ91-T6 and NZ30K₀₄-T6 alloys were also investigated. The results of the fatigue tests of the two alloys are plotted in Fig. 12a. The average fatigue strength (corresponding to 10^7 cycles) and the ratios of fatigue strength/yield strength ($\sigma_f/\sigma_{0.2}$), the ratios of fatigue strength/ultimate tensile strength (σ_f/σ_b) of these alloys are also calculated and summarized in Table 1. It can be seen that the NZ30K₀₄-T6 alloy shows a higher fatigue strength than the AZ91-T6 alloy when they have the same grain size. The average fatigue strength of the peak-aged NZ30K₀₄ alloy is ~ 89 MPa, which represents an approximate 20 % increase compared with the AZ91-T6 alloy (~ 74 MPa). In contrast, the two alloys exhibit the similar ratio values of $\sigma_f/\sigma_{0.2}$ (0.56–0.6) and ratio values of σ_f/σ_b (~ 0.32). The improvement in fatigue endurance limit in the T6-treated NZ30K₀₄ alloy can be attributed to matrix strength.

In this present study, the maximum stress amplitude of the AZ91-T6 and NZ30K₀₄-T6 alloys

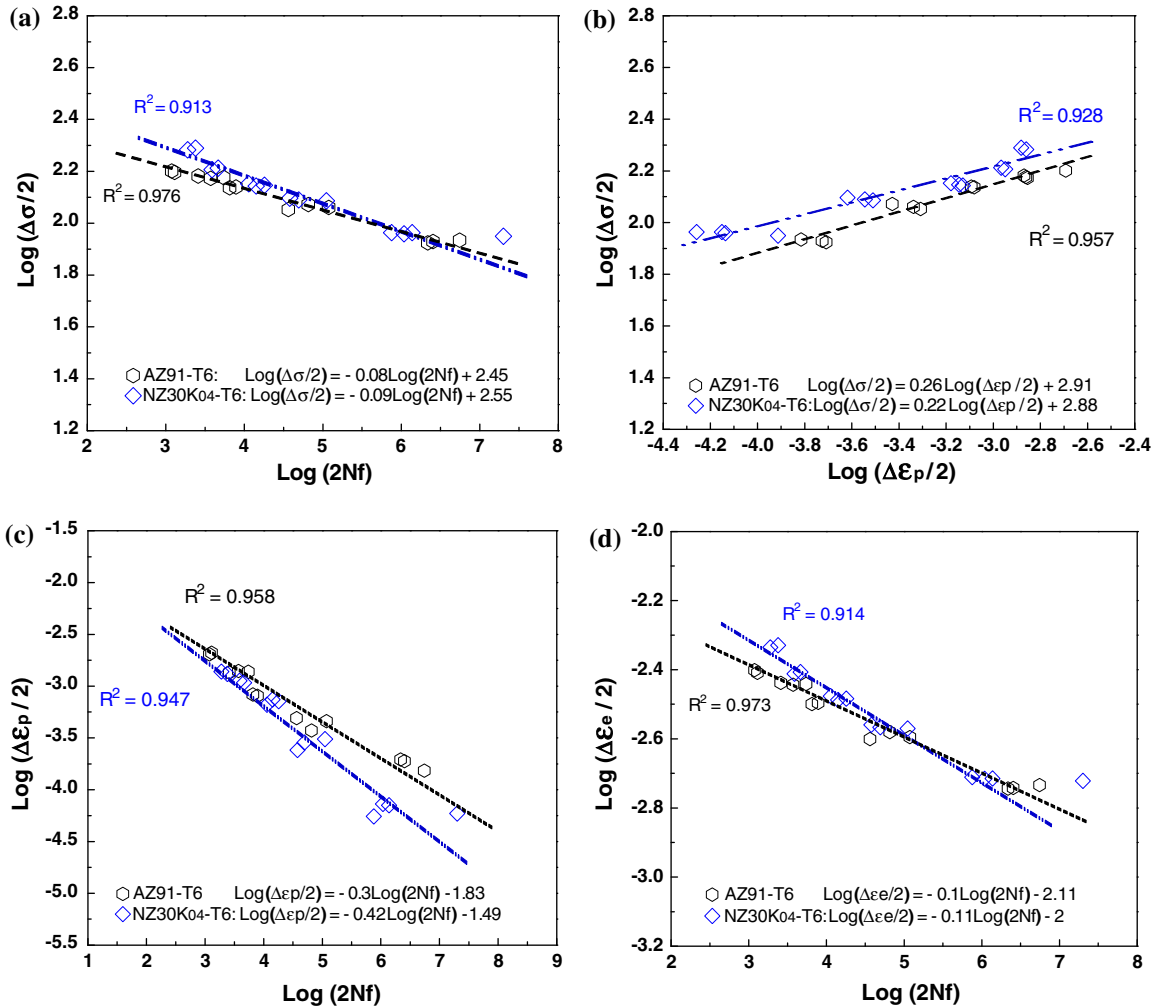


Figure 11 Evaluations of fatigue parameters for the AZ91D-T6 and NZ30K₀₄-T6 alloys: **a** log stress amplitude ($\Delta\sigma$) versus log number of reversals to failure ($2N_f$), **b** log stress amplitude ($\Delta\sigma$) versus log plastic strain amplitude ($\Delta\varepsilon_p$), **c** log elastic strain

amplitude ($\Delta\varepsilon_e$) versus log number of reversals to failure ($2N_f$), and **d** log plastic strain amplitude ($\Delta\varepsilon_p$) versus log number of reversals to failure ($2N_f$).

Table 4 Strain-controlled fatigue parameters of the AZ91D-T6 and NZ30K₀₄-T6 alloys

Alloys	Cyclic strain-hardening exponent, n'	Cyclic strength coefficient, K' (MPa)	Fatigue strength exponent, b	Fatigue ductility coefficient, ε_f' (%)	Fatigue ductility exponent, c	Fatigue strength coefficient, σ_f' (MPa)
AZ91D	0.26	813	-0.08	0.015	-0.3	282
NZ30K ₀₄	0.22	759	-0.09	0.032	-0.42	355

tested at strain-controlled loading is considered as the equivalent stress amplitude. The maximum stress amplitudes as a function of the number of cycles to failure for both AZ91-T6 and NZ30K₀₄-T6 alloys are shown in Fig. 12b. These results were also used to confirm the results of the fatigue life prediction models.

Fatigue crack initiation and crack propagation behaviors

The fatigue fracture surfaces of the AZ91-T6 and NZ30K₀₄-T6 alloy samples were carefully observed using a SEM. The SEM results, as exemplarily shown in Fig. 13, clearly indicate that the fatigue cracks in

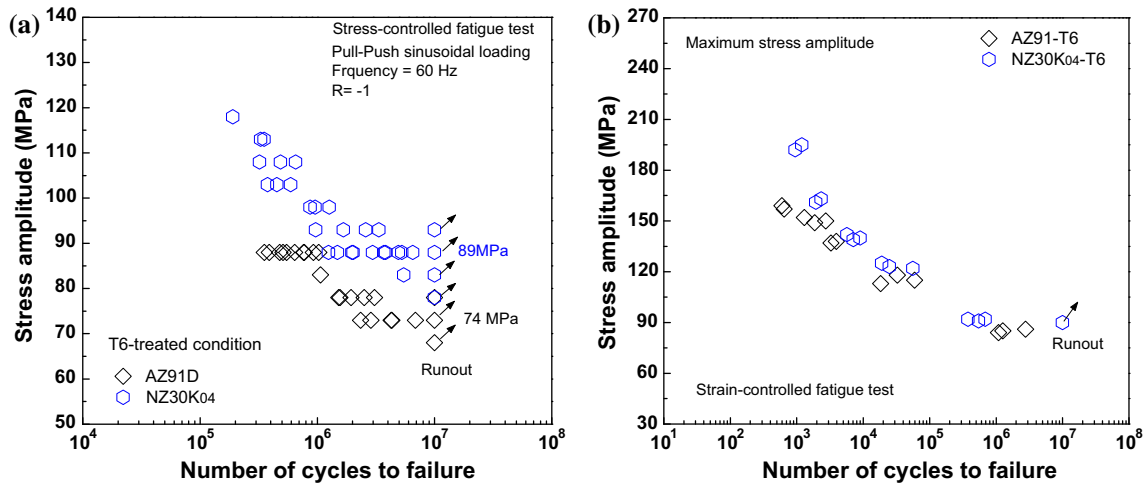


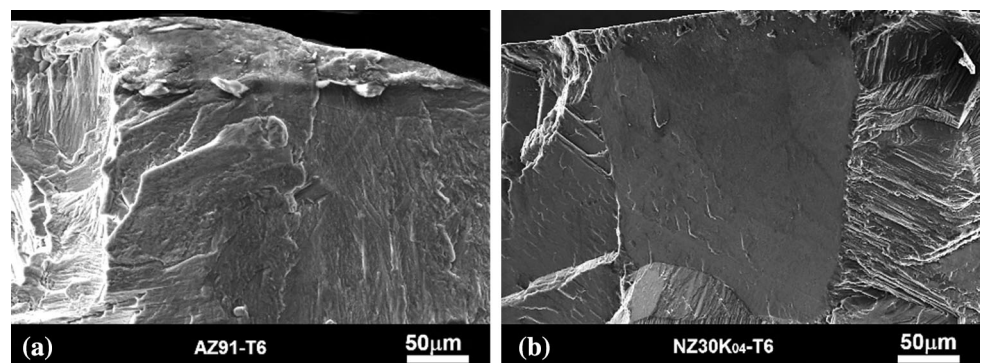
Figure 12 **a** Stress-life curves of the AZ91-T6 and NZ30K₀₄-T6 alloys. **b** Half-life stress amplitude as a function of the number of cycles to failure for both AZ91-T6 and NZ30K₀₄-T6 alloys.

the two alloy samples mainly originate from the grains located at or close to the sample surface. No casting defects including porosities, oxides, and inclusions can be observed in the crack initiation region of the fatigue samples. During fatigue testing, surface grains are the weakest and they deform plastically at the lowest stress leading to the formation of microcracks within the grain. For both AZ91 and NZ30K₀₄ alloys, the failure in the T6-treated samples is caused mainly by slip band cracking. For the samples tested at lower stress amplitude or total strain amplitude, fatigue cracks mainly initiate from a single site. Multiple fatigue crack origins, however, were also observed in the samples tested at higher total strain amplitude or stress amplitude. For both AZ91-T6 and NZ30K₀₄-T6 alloys, close to the crack formation site, some fine fatigue striations can be

seen (Fig. 14a, b). In the crack propagation region, a more faceted and serrated fracture surface was observed, as shown in Fig. 14c, d. The large facets are in the order of grain size, indicating that the cracks tend to preferentially grow in a transgranular mode by cutting straight across the grains. These serrated fatigue striations indicate typical cyclic crack propagation (opening) and retention (close) during cyclic deformation. Cracked slip bands within grains originate the fatigue cracks and also assist the fatigue crack propagation. For both AZ91-T6 and NZ30K₀₄-T6 alloys, the fracture surface has an extremely rough appearance with clear evidence of overload failure mechanisms, as shown in Fig. 15.

The microfractographic examinations indicated that the grains as crack initiation site were found at the origins of the fatigue cracks in all AZ91-T6 and

Figure 13 Fatigue cracks initiated from the persistence slip bands in the **a** AZ91D-T6 alloy and **b** NZ30K₀₄-T6 alloy (*images* was taken using SEI).



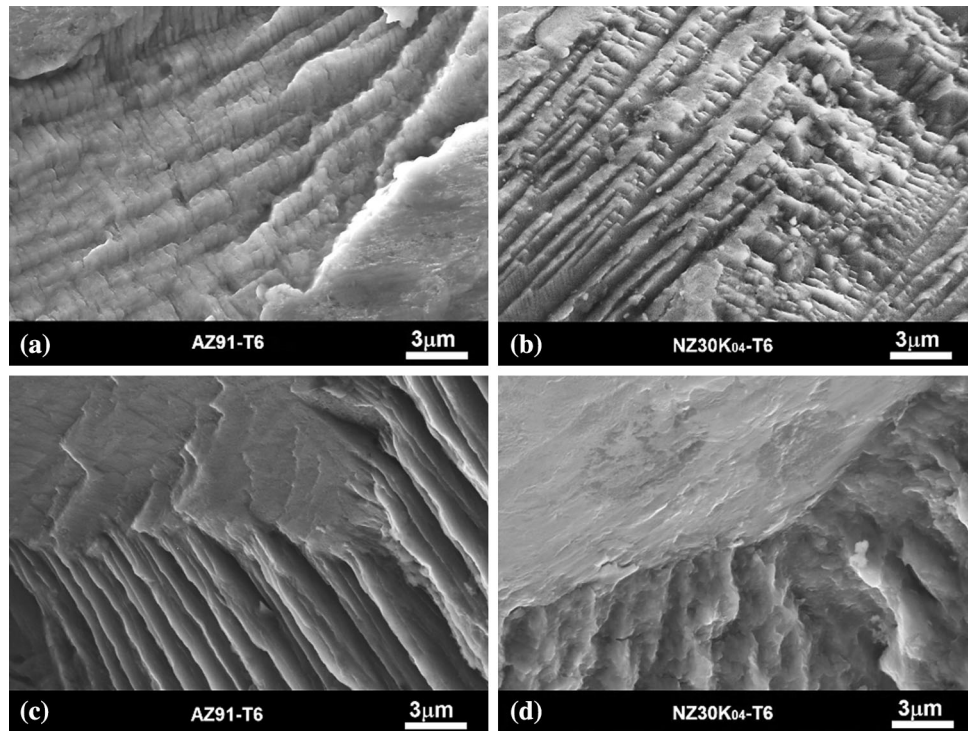


Figure 14 Typical secondary SEM images from the crack propagation region in the **a, c** AZ91-T6 alloy and **b, d** NZ30K₀₄-T6 alloy samples. The propagation region is characterized by **a, b** fine fatigue striations and **c, d** faceted surfaces and serrated propagation patterns.

NZ30K04-T6 alloy samples. Figure 16a shows the influence of grain size (i.e., the maximum ferret diameter of the grain size at the origin of the fatigue crack on the fatigue specimen fracture surface) on the fatigue life of both AZ91-T6 and NZ30K₀₄-T6 alloys tested at stress amplitudes of 88 MPa. It can be clearly seen that the fatigue life of two alloys increases with the decrease of the grain size as crack initiation site. It is believed that the variation and scatter of fatigue life is mainly attributed to the different sizes of the grains as crack initiation site. In order to discern which process (crack initiation or crack propagation) is dominant in determining total life, the ratios between crack initiation life and total life at different stress amplitudes were obtained and plotted in Fig. 16b. These results show that the total fatigue life of cast AZ91-T6 and NZ30K₀₄-T6 alloys is strongly controlled by the crack propagation process, especially at high stress/strain amplitude. Increasing the stress amplitude or strain amplitude can apparently reduce the fatigue crack initiation life of the alloy. It is also clearly seen that the NZ30K₀₄-T6 alloy samples show higher fatigue crack initiation lives than the AZ91-T6 alloy samples when they have the same grain sizes.

Application of multi-scale fatigue (MSF) life models

It has been reported that the fatigue life of the cast magnesium alloys failed by various crack initiation mechanisms (such as cracked slip bands and twinning initiating the cracks) can be predicted using the MSF life models together with the microstructure characteristics (such as grains) and the tensile properties [33]. For both AZ91-T6 and NZ30K₀₄-T6 alloys containing no porosities, persistent slip bands (PSB) which occurred within an individual grain close to the free surfaces of the samples would quickly propagate across the whole grain by flat cleavage mode and stop at the grain boundary. Slip bands can be effectively retarded by the grain boundaries from which high stress concentrations can be easily induced. Continuous cyclic loading leads to the formation of fatigue cracking in the localized damage areas such as slip bands [39, 49–52]. The cracked slip bands as crack initiation site are on the order of the grain sizes in these alloys, indicating that the grain size defines the slip distance for crack initiation. Both equivalent initial crack-like grain size and local equivalent plastic strain control the crack initiation

Figure 15 Typical secondary SEM images from the overloading region in the **a** AZ91-T6 alloy and **b** NZ30K₀₄-T6 alloy.

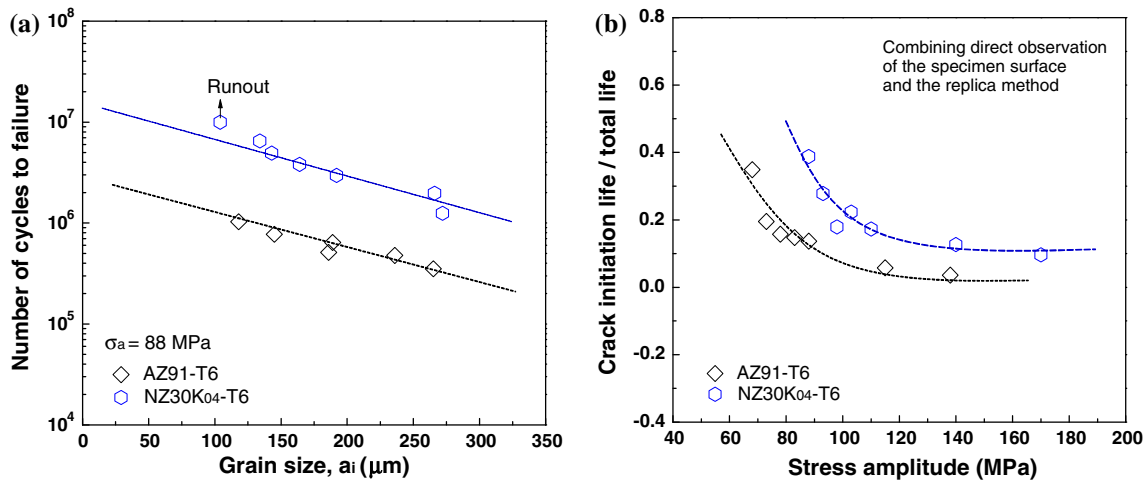
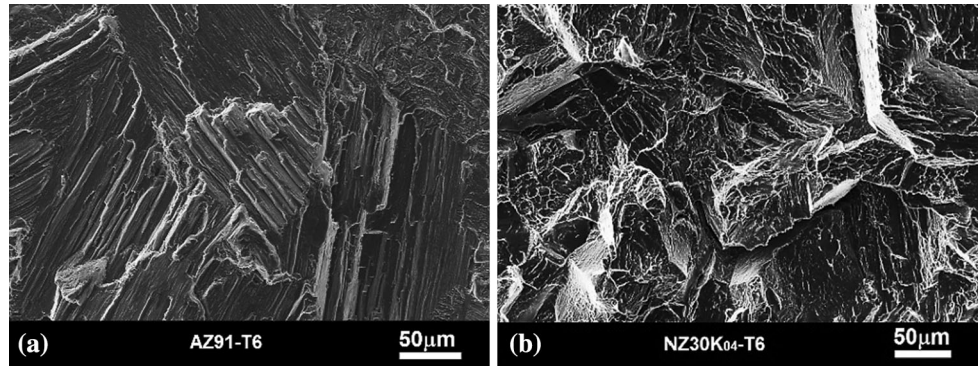


Figure 16 **a** Fatigue lives of the AZ91-T6 alloy and the NZ30K₀₄-T6 alloy, as a function of grain size as crack initiation site. **b** The ratios between crack initiation life and total life of the AZ91-T6 alloy and the NZ30K₀₄-T6 alloy, as a function of stress amplitudes.

life of these alloys. Therefore, the crack initiation life (N_i) of both AZ91-T6 and NZ30K₀₄-T6 alloys can be estimated by [32]:

$$N_i = C_1 (\Delta \epsilon_{eq}^p)^{-g} (d_g)^h, \tag{4}$$

where C_1 , g , and h are material-related constants; $\Delta \epsilon_{eq}^p$ is local equivalent plastic strain; d_g is the equivalent initial crack-like grain size.

For both AZ91-T6 and NZ30K₀₄-T6 alloys, the cracks in crack initiation region and growth region tend to propagate along the cracked slip bands and cut straight across the grains. As a result, only cracked slip bands can provide an easy path for crack propagation. Consequently, the grain size is the characteristic microstructure feature constraining slip distance for crack propagation. The cycles to propagate the crack from one grain size to final failure (N_p) can be estimated by the short crack model. Based on the crack-tip opening displacement (CTOD) theory,

Frost et al. [53] and Nistani et al. [54] suggested that the propagation rate of a small crack can be estimated as:

$$\frac{da}{dN} = C_3 \sigma_a^n \cdot a \tag{5}$$

Considering the influence of material properties (such as yield strength or ultimate tensile strength), Eq. 5 is modified by Nisitani et al. [54] as:

$$\frac{da}{dN} = C_4 \left(\frac{\sigma_a}{\sigma_b} \right)^n \cdot a \tag{6}$$

Here C_3 and n are constants, σ_a and a are the initiation crack size and stress amplitude, respectively; σ_b can be either yield strength (σ_{ys}) or ultimate tensile strength (σ_{UTS}). To account for global strain condition of a material in addition to the crack-tip plasticity, Caton et al. [55] further proposed that the propagation rate of a small crack can be calculated by:

$$\frac{da}{dN} = C_5 \left(\varepsilon_{\max} \cdot \frac{\sigma_a}{\sigma_{ys}} \right)^n \cdot a, \tag{7}$$

where ε_{\max} is the maximum total strain during loading cycle. Following integration of Eq. 7 and taking N_p ($=N_f - N_i$) as the number of cycles to propagate a crack of size a_i to failure, the relationship between fatigue life and initial crack size as well as material properties (σ_{ys}) is expressed as:

$$\ln \frac{a_f}{a_i} = C_6 \left(\varepsilon_{\max} \cdot \frac{\sigma_a}{\sigma_{ys}} \right)^n \cdot N_p, \tag{8}$$

where a_f is the final crack size. Therefore, the crack propagation life of both AZ91-T6 and NZ30K04-T6 alloys is mainly determined by the equivalent initial crack-like grain size, applied stress amplitude, yield strength or ultimate tensile strength of the materials, and maximum total strain during loading cycle. The fatigue crack propagation life can thus be estimated by [32]:

$$N_p = C_2 \left(\varepsilon_{\max} \sigma_a \sigma_{ys}^{-1} \right)^n d_g^q \tag{9}$$

The total fatigue life can be calculated by [32]:

$$N = C_1 \left(\Delta \varepsilon_{eq}^p \right)^{-g} (d_g)^h + C_2 \left(\varepsilon_{\max} \sigma_a \sigma_{ys}^{-1} \right)^n (d_g)^q \tag{10}$$

Here C_1 , C_2 , g and h , n , and q are the material-related constants; $\Delta \varepsilon_{eq}^p$ is the local equivalent plastic strain; σ_a is the stress amplitude; σ_{ys} is the yield strength; ε_{\max} is the maximum total strain during loading cycle; d_g is the equivalent initial crack-like grain size. The maximum total strain ε_{\max} is determined from the true stress–true strain curves of cast magnesium alloys in the monotonic loading condition, as shown in Fig. 8b. The local equivalent plastic strain can be estimated using

$$\Delta \varepsilon_{eq}^p = \varepsilon_{\max} - \frac{\sigma_a}{E}, \tag{11}$$

where E is the Young’s modulus (modulus of elasticity, for cast magnesium alloys is 30–50 MPa).

In our previous work [33], the experiment results of tensile properties and push–pull high cycle fatigue life of the NZ30K₁ (Mg–3Nd–0.2Zn–1Zr, grain size $d \sim 69 \mu\text{m}$) alloy were used to develop the MSF life models and obtain the model parameters ($C_1 \approx 16$, $g \approx 1.53$, $h \approx -0.77$, $C_2 \approx 0.41$, $n \approx -2.84$ and $q \approx -0.73$). Concerning the similar crack initiation and crack propagation mechanisms between NZ30K-T6 and AZ91-T6 alloys, it is expected that the same model parameter for the NZ30K₁-T6 alloy can also be

used to predict the fatigue life of cast AZ91-T6 and NZ30K₀₄-T6 alloys failed by cracked slip bands. In this work, the MSF life models for both AZ91-T6 and NZ30K₀₄-T6 alloys is suggested by Eq. 12 accounting for the effect of grain size:

$$N = \left(C_1 \left(\Delta \varepsilon_{eq}^p \right)^{-g} (d_g)^h + C_2 \left(\varepsilon_{\max} \sigma_a \sigma_{ys}^{-1} \right)^n (d_g)^q \right) * (d_0/d_g), \tag{12}$$

where d_0 is the average size of the NZ30K₁-T6 alloy ($\approx 69 \mu\text{m}$), d_g is the average size of other cast magnesium alloys.

For comparison, Fig. 17 shows the predicted fatigue life of both AZ91-T6 and NZ30K₀₄-T6 alloys failed from cracked slip bands (using Eq. 12) and the measured actual fatigue life. It should be noted that the predicted fatigue life shown in the figure is based on the maximum ferret diameter of the grain size at the origin of the fatigue crack on the fatigue specimen fracture surface. Given the inherent scatter of fatigue life data, it is believed that predictions within an order of magnitude of measured values are useful. Figure 18 compares the calculated fatigue life curves for the AZ91-T6 and NZ30K₀₄-T6 alloy samples failed from cracked slip bands using MSF life model to the actual fatigue life. The upper, median, and lower solid lines represent the fatigue life curves predicted based on MSF life model with the minimum, average, and maximum size values of grain as crack initiation site, respectively. Solid lines in Fig. 18 represent total calculated fatigue life consisting of initiation life (N_i) and propagation life (N_p) which are shown as dashed

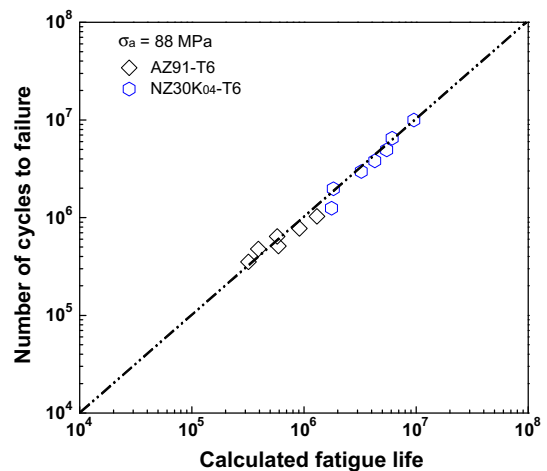


Figure 17 Comparison of the actual fatigue life with the calculated fatigue life for the AZ91-T6 alloy and the NZ30K₀₄-T6 alloy.

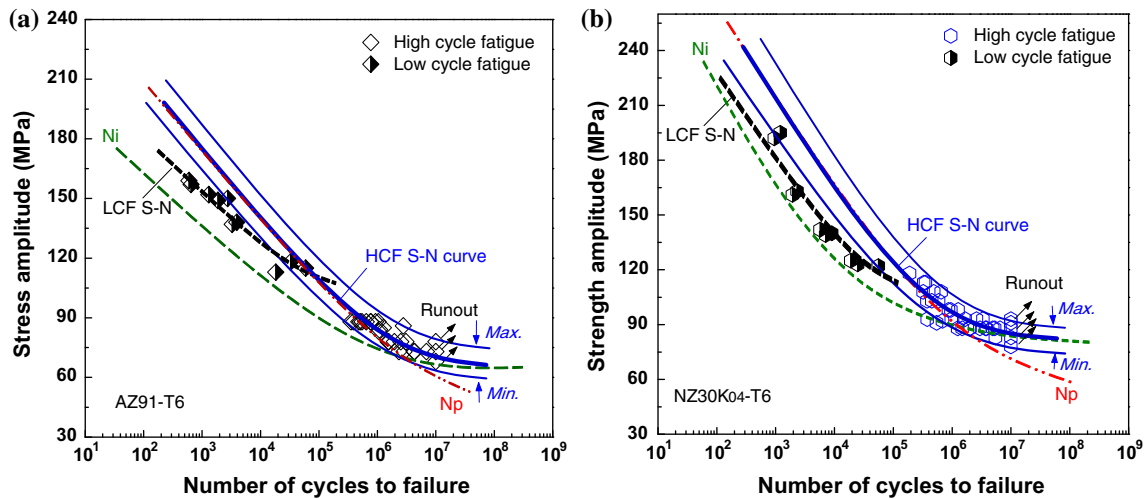


Figure 18 High cycle fatigue (HCF $>10^5$) S–N curve of the **a** AZ91-T6 alloy and **b** NZ30K₀₄-T6 alloy together with the prediction of MSF life models (Eq. 12) using the grain sizes of minimum, average, and maximum as fatigue crack initiation sites.

lines. The total fatigue life curves, the crack initiation life (N_i) curves, and the crack propagation life (N_p) curves in Fig. 18 were obtained by using Eq. 12 and related model parameters ($d_g \sim 135 \mu\text{m}$ and $d_0 \sim 69 \mu\text{m}$). The results indicate clearly that the predicted fatigue life based on Eq. 12 (MSF life models) is in good agreement with the actual fatigue life. By considering the probabilistic distribution of characteristic microstructures (such as grain size), the MSF life model (Eq. 12) can accurately predict the variation and scatter of the fatigue life data. However, we came short in directly applying the MSF life to LCF lives of both AZ91-T6 and NZ30K₀₄-T6 alloys (as shown in Fig. 18). This is probably due to a fact that the crack propagation life occupies the most of the fatigue life in LCF region. In contrast, as shown in Fig. 18, Coffin–Manson law and Basquin equation (Eq. 3) which is related to the crack propagation process can be used to estimate the LCF life of two alloys.

Conclusion

(1) When the two alloys have the same grain size, the NZ30K₀₄-T6 alloy exhibits higher mechanical properties (YS of ~ 148 MP, UTS of ~ 284 MPa, elongation of ~ 7.2 %, and FS of ~ 89 MPa), improved by about 13 % in YS,

Low cycle fatigue (LCF) S–N curve of the **a** AZ91-T6 alloy and **b** NZ30K₀₄-T6 alloy together with the prediction of Coffin–Manson law and Basquin equation (Eq. 3) are also shown in the figures.

18 % in UTS, 50 % in elongation, and 20 % in FS, respectively, compared with those of the AZ91-T6 alloy. The NZ30K₀₄ alloy also shows an increase in cyclic stress amplitude in comparison with the AZ91-T6 alloy. The higher cyclic stress amplitude, tensile, and fatigue properties of the NZ30K₀₄-T6 alloy are mainly attributed to the improved matrix strength from the higher precipitate strengthening contributions in this alloy.

(2) For the AZ91-T6 alloy, cyclic hardening to saturation controlled by dislocation slip easily occurs, which is mainly influenced by grain boundaries and large discontinuous precipitates. The cyclic stress amplitude of the NZ30K₀₄-T6 alloy first increases and then decreases with the increase of the number of cycles, indicating that dislocations tend to bypass the precipitates by the shearing mechanism. For the AZ91-T6 alloy and the NZ30K₀₄-T6 alloy, symmetrical hysteresis loops at all total strain amplitudes indicate that Bauschinger effect was not pronounced. For these alloys, the dependence of fatigue parameters on the fatigue life obeys the Coffin–Manson law and Basquin equation.

(3) Fatigue failure of both AZ91-T6 and NZ30K₀₄-T6 alloys mainly originates from the grains located close to or at the specimen-free surface.

The cracked slip bands initiate the fatigue crack and also assist the fatigue crack propagation.

- (4) High cycle fatigue lives of both AZ91-T6 and NZ30K₀₄-T6 alloys without casting defects also can be quantitatively predicted using MSF life models and the same model parameters. The variation and scatter of fatigue S–N data can be estimated by MSF life models with extreme statistic values of grain size in the materials. The Coffin–Manson law and Basquin equation can be used to evaluate the LCF lives of two alloys.

Acknowledgements

This work was supported by the Project Funded by China Postdoctoral Science Foundation (2015M571562). The authors are grateful to Prof. Qigui Wang (GM), Prof. Alan A. Luo (Ohio State University), Profs. Wenjiang Ding, Liming Peng, and Dayong Li, and Drs. Penghuai Fu and Yingxin Wang (SJTU) for their helpful discussions.

References

- Taub AI, Krajewski PE, Luo AA, Owens JN (2007) The evolution of technology for materials processing over the last 50 years: the automotive example. *JOM* 59(2):48–57
- Luo AA (2004) Recent magnesium alloy development for elevate temperature applications. *Int Mater Rev* 49:13–30
- Mayer H, Papakyriacou M, Zettl B, Stanzl-Tschegg SE (2003) Influence of porosity on the fatigue limit of die cast magnesium and aluminum alloys. *Int J Fatigue* 25:245–256
- Horstemeyer MF, Yang N, Gall K, McDowell DL, Fan J, Gullett PM (2004) High cycle fatigue of a die cast AZ91E-T4 magnesium alloy. *Acta Mater* 52:1327–1336
- Fu PH, Peng LM, Jiang HY, Chang JW, Zhai CQ (2008) Effects of heat treatments on the microstructures and mechanical properties of Mg-3Nd-0.2Zn-0.4Zr (wt%) alloy. *Mater Sci Eng A* 486:183–192
- Fu PH, Peng LM, Jiang HY, Ma L, Zhai CQ (2008) Chemical composition optimization of gravity cast Mg-yNd-xZn-Zr alloy. *Mater Sci Eng A* 496:177–188
- Li ZM, Wang QG, Luo AA, Peng LM, Fu PH, Wang YX (2013) Effects of grain size and heat treatment on the tensile properties of Mg-3Nd-0.2Zn magnesium alloys. *Mater Sci Eng A* 582:170–177
- Li ZM, Wang QG, Luo AA, Fu PH, Peng LM, Wang YX, Wu GH (2013) High cycle fatigue of cast Mg-3Nd-0.2Zn magnesium alloys. *Metall Mater Trans A* 44:5202–5215
- Peng LM, Fu PH, Li ZM, Yue HY, Li DY, Wang YX (2014) High cycle fatigue behaviors of low pressure cast Mg-3Nd-0.2Zn-2Zr alloys. *Mater Sci Eng A* 611:170–176
- Peng LM, Fu PH, Li ZM, Wang YX, Jiang HY (2014) High cycle fatigue properties of cast Mg-xNd-0.2Zn-Zr alloys. *J Mater Sci* 49:7105–7115. doi:10.1007/s10853-014-8417-7
- Li ZM, Wang QG, Luo AA, Fu PH, Peng LM (2015) Fatigue strength dependence on the ultimate tensile strength and hardness in magnesium alloys. *Int J Fatigue* 80:468–476
- Chang JW, Peng LM, Guo XW, Atrens A, Fu PH (2008) Comparison of the corrosion behavior in 5 % NaCl solution of Mg alloys NZ30K and AZ91D. *J Appl Electrochem* 38:207–214
- Chang JW, Guo XW, Fu PH, Peng LM, Ding WJ (2007) Effect of heat treatment on corrosion and electrochemical behavior of Mg-3Nd-0.2Zn-0.4Zr (wt%) alloy. *Electrochim Acta* 52:3160–3167
- Chang JW, Fu PH, Guo XW, Peng LM (2007) The effects of heat treatment and zirconium on the corrosion behavior of Mg-3Nd-0.2Zn-0.4Zr (wt%) alloy. *Corros Sci* 49:2612–2627
- Li ZM, Wang QG, Luo AA, Peng LM, Fu PH, Wang YX (2013) Improved high cycle fatigue properties of a new magnesium alloy. *Mater Sci Eng* 582:170–177
- Begum S, Chen DL, Xu S, Luo AA (2008) Strain-controlled low-cycle fatigue properties of a newly developed extruded magnesium alloy. *Metall Mater Trans A* 39:3014–3026
- Begum S, Chen DL, Xu S, Luo AA (2009) Low cycle fatigue properties of an extruded AZ31 magnesium alloy. *Int J Fatigue* 31:726–735
- Li QZ, Yu Q, Zhang JX, Jiang YY (2010) Effect of strain amplitude on tension-compression fatigue behavior of extruded Mg₆Al₁ZnA magnesium alloy. *Scr Mater* 62:778–781
- Gall K, Horstemeyer MF, Degner BW, McDowell DL, Fan J (2001) On the driving force for fatigue crack formation from inclusions and voids. *Int J Fract* 108:207–233
- Xu DK, Liu L, Xu YB, Han EH (2007) The crack initiation mechanism of forged Mg-Zn-Y-Zr alloy in the super-long fatigue regime. *Scr Mater* 56:1–4
- Li ZM, Fu PH, Peng LM, Wang YX, Jiang HY, Wu GH (2013) Comparison of high cycle fatigue behaviors of Mg-3Nd-0.2Zn-Zr alloy prepared by different casting processes. *Mater Sci Eng A* 579:170–179
- Wang QG, Davidson CJ, Griffiths JR, Crepeau PN (2006) Oxide films, pores and the fatigue lives of cast aluminum alloys. *Metall Mater Trans B* 44:887–895
- Wang QG, Jones PE (2007) Prediction of fatigue performance in aluminum shape castings containing defects. *Metall Mater Trans B* 38:615–621
- Xu DK, Liu L, Xu BY, Han EH (2008) The fatigue behavior of I-phase containing as-cast Mg-Zn-Y-Zr alloy. *Acta Mater* 56:985–994

- [25] Wang QG, Apelian D, Lados DA (2001) Fatigue behavior of A356-T6 aluminum cast alloys. Part I. Effect of casting defects. *J Light Met* 1:73–84
- [26] De PS, Mishra RS, Smith CB (2009) Effect of microstructure on fatigue life and fracture morphology in an aluminum alloy. *Scr Mater* 60:500–503
- [27] Li ZM, Fu PH, Peng LM, Becker EP, Wu GH (2013) Influence of solution temperature on fatigue behavior of AM-SC1 cast magnesium alloy. *Mater Sci Eng A* 565:250–257
- [28] Wang QG, Apelian D, Lados DA (2001) Fatigue behavior of A356/357 aluminum cast alloys. Part II—effect of microstructural constituents. *J Light Met* 1:85–97
- [29] Siddiqui RA, Abdul-Wahab SA, Pervez T (2008) Effect of aging time and aging temperature on fatigue and fracture behavior of 6063 aluminum alloy under seawater influence. *Mater Des* 29:70–79
- [30] Burba ME, Caton MJ, Jha SK, Szczepanski CJ (2013) Effect of aging treatment on fatigue behavior of an Al-Cu-Mg-Ag alloy. *Metal Mater Trans A* 44(11):4954–4967
- [31] Davidson CJ, Griffiths JR, Machin AS (2002) The effect of solution heat-treatment time on the fatigue properties of an Al-Si-Mg casting alloy. *Fatigue Fract Eng Mater Struct* 25(2):223–230
- [32] Wang QG, Jones P (2011) Fatigue life prediction in aluminum shape castings. *SAE Int J Mater Manuf* 4:289–297
- [33] Li ZM, Wang QG, Luo AA, Peng LM, Zhang P (2015) Fatigue behavior and life prediction of cast magnesium alloys. *Mater Sci Eng A* 647:113–126
- [34] Fu PH, Peng LM, Jiang HY, Zhai CQ, Gao X, Nie JF (2007) Zr-containing precipitates in Mg-3Nd-0.2Zn-0.4Zr Alloy during solution treatment at 540 °C. *Mater Sci Forum* 546–549:97–100
- [35] Tang W, Han EH, Xu YB, Liu L (2005) Effect of heat treatment on microstructure and properties of AZ80 magnesium alloy. *Acta Metal Sin* 41(11):1199–1206
- [36] Yin SM, Yang F, Yang XM, Wu SD, Li SX, Li GY (2008) The role of twinning-detwinning on fatigue fracture morphology of Mg-3 %Al-1 %Zn alloy. *Mater Sci Eng A* 494:397–400
- [37] Wu L, Jain A, Brown DW, Stoica GM, Agnew SR, Clausen B, Fielden DE, Liaw PK (2008) Twinning-detwinning behavior during the strain-controlled low-cycle fatigue testing of a wrought magnesium alloy ZK60A. *Acta Mater* 56:88–95
- [38] Lou XY, Li M, Boger PK, Agnew SR, Wagoner RH (2007) Hardening evolution of AZ31B Mg sheet. *Int J Plast* 23:44–86
- [39] Wu YJ, Zhu R, Wang JT, Ji WQ (2010) Role of twinning and slip in cyclic deformation of extruded Mg-3 %Al-1 %Zn alloys. *Scr Mater* 63:1077–1080
- [40] Fu PH, Peng LM, Nie JF, Jiang HY, Ma L, Bourgeois L (2011) Ductility improvement of Mg-Nd-Zr cast by trace addition of Zn. *Mater Sci Forum* 690:230–233
- [41] Cáceres CH, Davidson CJ, Griffiths JR, Newton CL (2002) Effects of solidification rate and ageing on the microstructure and mechanical properties of AZ91 alloy. *Mater Sci Eng* 325:344–355
- [42] Manson SS (1953) Behavior of materials under conditions of thermal stress. NACA TN-2933:105
- [43] Coffin LF (1954) A study of the effects of cyclic thermal stress in a ductile metal. *Trans ASME* 76:931–950
- [44] Hasegawa S, Tsuchida Y, Yano H, Matsui M (2007) Evaluation of low cycle fatigue life in AZ31 magnesium alloy. *Int J Fatigue* 29:1839–1845
- [45] Saitova LR, Höppel HW, Göken M, Semanova IP, Valiev RZ (2009) Cyclic deformation behavior and fatigue lives of ultrafine-grained Ti-6Al-4V ELI alloy for medical use. *Int J Fatigue* 31:322–331
- [46] Basquin OH (1910) The experimental law of endurance tests. *Proc ASTM* 10:625–630
- [47] Morrow JD (1965) Cyclic plastic strain energy and fatigue of metals. In: Internal friction, damping and cyclic plasticity. *ASTM STP* 378:45–87
- [48] Landgraf RW (1970) The resistance of metals to cyclic deformation. In: Achievement of high fracture resistance in metals and alloys. *ASTM STP* 467:33–36
- [49] Harvey SE, Marsh PG, Gerberich WW (1994) Atomic force microscopy and modeling of fatigue crack initiation in metals. *Acta Metall Mater* 42:3493–3502
- [50] Man J, Petreñec M, Obrtlík K, Polák J (2004) AFM and TEM study of cyclic slip localization in fatigued ferritic X10CrAl24 stainless steel. *Acta Mater* 52:5551–5561
- [51] Man J, Obrtlík K, Blochwitz C, Polák J (2002) Atomic force microscopy of surface relief in individual grains of fatigued 316 l austenitic stainless steel. *Acta Mater* 50:3767–3780
- [52] Polák J, Man J, Vystavel T, Petreñec M (2009) The shape of extrusions and intrusions and initiation of stage I fatigue cracks. *Mater Sci Eng A* 517:204–211
- [53] Frost NE, Dugdale DS (1958) The propagation of fatigue cracks in sheet specimens. *J Mech Phys Solids* 6:92–110
- [54] Nisitani H, Goto M, Kawagoishi N (1992) A small-crack growth law and its related phenomena. *Eng Fract Mech* 41(4):499–513
- [55] Caton MJ, Jones JW, Boileau JM, Allison JE (1999) The effect of solidification rate on the growth of small fatigue cracks in a cast 319-type aluminum alloy. *Metall Mater Trans A* 30A:3055–3068